



Radiation response of ODS ferritic steels with different oxide particles under ion-irradiation at 550 °C

Peng Song ^{a,*}, Daniel Morrall ^a, Zhexian Zhang ^b, Kiyohiro Yabuuchi ^b, Akihiko Kimura ^b

^a Graduate School of Energy Science, Kyoto University, Yoshida-honmachi, Sakyou-ku, Kyoto, 606-8501, Japan

^b Institute of Advanced Energy, Kyoto University, Gokasho, Uji, Kyoto, 611-0011, Japan

H I G H L I G H T S

- Morphology of oxide particle dispersion, rather than the O/M interface structure, is the main factor to suppress swelling.
- No hardening is induced in the three ODS steels irradiated with both single Fe³⁺ and dual (Fe³⁺ and He⁺) ions at 550 °C.
- Negligible hardening by He bubbles is probably due to their high fractions (~74%–82%) adjacent to the oxide particles.

A R T I C L E I N F O

Article history:

Received 27 October 2017

Received in revised form

4 January 2018

Accepted 4 February 2018

Available online 6 February 2018

Keywords:

Helium bubbles
Swelling
Softening
Oxide particles
Sink strength
ODS ferritic steels

A B S T R A C T

In order to investigate the effects of oxide particles on radiation response such as hardness change and microstructural evolution, three types of oxide dispersion strengthened (ODS) ferritic steels (named Y-Ti-ODS, Y-Al-ODS and Y-Al-Zr-ODS), mostly strengthened by Y-Ti-O, Y-Al-O and Y-Zr-O dispersoids, respectively, were simultaneously irradiated with iron and helium ions at 550 °C up to a damage of 30 dpa and a corresponding helium (He) concentration of ~3500 appm to a depth of 1000–1300 nm. A single iron ion beam irradiation was also performed for reference. Transmission electron microscopy revealed that after the dual ion irradiation helium bubbles of 2.8, 6.6 and 4.5 nm in mean diameter with the corresponding number densities of 1.1×10^{23} , 2.7×10^{22} and $3.6 \times 10^{22} \text{ m}^{-3}$ were observed in Y-Ti-ODS, Y-Al-ODS and Y-Al-Zr-ODS, respectively, while no such bubbles were observed after single ion irradiation. About 80% of intragranular He bubbles were adjacent to oxide particles in the ODS ferritic steels. Although the high number density He bubbles were observed in the ODS steels, the void swelling in Y-Ti-ODS, Y-Al-ODS and Y-Al-Zr-ODS was still small and estimated to be 0.13%, 0.53% and 0.20%, respectively. The excellent swelling resistance is dominantly attributed to the high sink strength of oxide particles that depends on the morphology of particle dispersion rather than the crystal structure of the particles. In contrast, no dislocation loops were produced in any of the irradiated steels. Nanoindentation measurements showed that no irradiation hardening but softening was found in the ODS ferritic steels, which was probably due to irradiation induced dislocation recovery. The helium bubbles in high number density never contributed to the irradiation hardening of the ODS steels at these irradiation conditions.

© 2018 Elsevier B.V. All rights reserved.

1. Introduction

Oxide dispersion strengthened (ODS) steels owe their high performance to the ultrahigh density of nanoscale oxides and fine grains. Because of their superior tensile, creep and fatigue strength at elevated temperatures [1,2] and excellent neutron radiation

tolerance [3], ODS steels can be used as a fusion blanket structural material to elevate the operating temperature and the overall thermal efficiency of fusion plants [4]. In addition, ODS ferritic steels with sufficient Al addition, which possess high corrosion/oxidation resistance, have been considered as a candidate fuel cladding for the next generation fission reactors [1,5] and light water reactors with accident tolerant fuel [6]. In harsh nuclear service environments, especially in fusion components, helium atoms generated through (n, α) nuclear reactions or directly from in-core plasma lead to the formation of interstitial helium atoms and helium-vacancy clusters, such as helium bubbles or voids in

* Corresponding author. Institute of Advanced Energy, Kyoto University, Gokasho, Uji, Kyoto 611-0011, Japan.

E-mail address: p-song@iae.kyoto-u.ac.jp (P. Song).

structural materials, which may result in the degradation of mechanical properties, such as hardening and embrittlement, as well as swelling [7].

Concerning ODS steels, it is commonly accepted that helium effects are mitigated by numerous dispersed oxide particles, acting as effective sinks providing sites for defect accumulation, combination or annihilation [3,4]. Previous studies confirmed the trapping effects of oxide particles on nanometer-sized cavities by means of transmission electron microscopy (TEM) [8], scanning TEM [9,10] and atom probe tomography (APT) [11] after various types of irradiations and post-irradiation annealing treatments in the temperature range of 400–750 °C. Meanwhile, two dominating nucleation styles of cavities in association with oxides were suggested by G.R. Odette [12]: one is the oxide particle that contains cavities and the other is the oxide particle attached with cavities in a side to side way. To our knowledge, the former was only found in amorphous Y-Al-O particles [13]. The previous experimental results revealed that not only oxide particle/matrix (O/M) interfaces could provide preferential nucleation sites for cavities, but also the oxides themselves might have some solubility for helium or helium bubbles. The effect of oxide type on the helium solubility was investigated by related simulation studies on various oxides (e.g. Y-Ti-O, Y-Al-O oxides) [14,15]. Finally, as expected, He-induced swelling was effectively suppressed by oxide particles and was well demonstrated by comparing ODS steels and non-ODS steels [16,17]. Ion-irradiation experiments of ODS steels with different oxide particle types, sizes and number densities were mainly studied by single He ion irradiations at relatively low displacement damages, indicating that finer oxide particles with a higher number density contributed to a smaller swelling [18,19]. Regarding the effect of simultaneous dual beam (Fe and He ions) irradiation, the amount of research is limited.

As for the peak swelling temperature, several previous studies indicated that the swelling in ferritic/martensitic (F/M) alloys peaked at around 420–470 °C in ion irradiations [20] and neutron irradiations [21] and is affected by the damage rate. Since helium may reduce the mobility of vacancies and increase the stability of voids, helium effects are expected to be enhanced at a higher temperature than 470 °C. In the previous research on helium effects in ODS ferritic steels, the targeted irradiation temperatures were ranging up to 700 °C and the maximum swelling rate was at 500–600 °C [22] because the mobility of helium might also become larger at these high temperatures [23]. It is considered that the peak swelling is determined as a result of a balance between the mobility of vacancies and thermal stability of voids.

Helium-induced hardening is another key concern for the structural materials in fusion systems. At room temperature, the implantation of about 750 appm He to an ODS ferritic steel gave rise to an obvious hardening of 21% with homogeneously distributed helium nanobubbles [24]. Likewise, hardening became larger with increasing helium concentration obeying a 1/2-power law [25]. But in another ODS ferritic steel implanted with about 3400 appm He, as the temperature increased from 100 to 500 °C, hardening decreased continuously from ~15% to ~3.5% [22]. These results elucidated that the hardening behavior was affected by implantation temperature and even materials. Furthermore, the difference in hardening between single Fe ion and dual (Fe and He) ion beam irradiations was significantly influenced by irradiation temperature: at 300 °C, the hardening caused by dual beam irradiation was evidently larger than that by single Fe ion irradiation [26], while at 500 °C, the hardening was almost the same between the two [27]. A simulation study indicated that helium bubbles of 2 nm in diameter with more than 5 helium atoms per vacancy were strong obstacles to the glide motion of an edge dislocation in iron [28], and

significant hardening has been observed in reduced-activation ferritic/martensitic (RAFM) steels irradiated up to 11.3 dpa/1175 appm He in the Swiss Spallation Neutron Source (SINQ) [29]. In contrast to these hardening effect of helium, R. Kasada et al. reported that the hardening induced by helium ion irradiation (580 at. ppm He/0.226 dpa at below 423 K) in a reduced-activation martensitic steel was interpreted simply in terms of displacement damage, suggesting that there is no significant effect of helium on the hardening [30]. Therefore, in fusion relevant temperature region (~400–700 °C for F/M steel) [31], helium effects on irradiation hardening are still uncertain.

Since the material performance of ODS steels depends on the morphology of oxide particle dispersion, dispersion control is essential for development of the steel. The Al-addition to FeCr-ODS steels altered the main particles from Y₂Ti₂O₇ pyrochlore to YAH and YAP [32], and a small additions of Zr to FeCrAl ODS steels altered the majority of oxide particles from Y-Al-O dispersoids to Y-Zr-O dispersoids [33], resulting in an enhanced high-temperature strength of the steel [1].

In this research, we investigated the radiation response of three types of ODS ferritic steels mostly strengthened by Y-Ti-O, Y-Al-O and Y-Zr-O oxides, respectively, focusing on the roles of helium implantation in the hardness change and swelling under dual beam irradiation at 550 °C.

2. Experimental

2.1. Materials

The materials used in this research were three types of ODS ferritic steels, Fe-13.6Cr-1.9W-0.16Ti-0.33Y₂O₃ (Y-Ti-ODS), Fe-15.42Cr-3.8Al-1.85W-0.1Ti-0.36Y₂O₃ (Y-Al-ODS) and Fe-14.59Cr-3.46Al-1.84W-0.14Ti-0.27Zr-0.33Y₂O₃ (Y-Al-Zr-ODS), which were produced by mechanical alloy processing. After hot extrusion and forging were performed at 1150 °C, the materials were finally annealed at 1150 °C for 1 h and followed by air-cooling. More details of the material conditions and processing were described in Refs. [19,33,34].

Specimens were sampled so that the specimen surface was perpendicular to the extrusion direction. Specimen surface was mechanically ground with SiC papers, and subsequently polished with successive grades of diamond spray down to 0.25 μm. Finally, electrolytic polishing was conducted in a solution of 10% (vol.) HClO₄ and 90% (vol.) CH₃COOH at room temperature except for Y-Al-ODS.

2.2. Irradiation conditions

Specimens were simultaneously irradiated with 6.4 MeV Fe³⁺ and 1 MeV He⁺ at the DuET facility in Kyoto University [35]. A single Fe³⁺ irradiation was also carried out for comparison. The beams were raster scanned at a frequency of 1000 Hz in a horizontal direction and 300 Hz in a vertical direction. In the dual beam irradiation, the He⁺ beam was declined with 45° to the normal of the specimen surface and maintained a simultaneous injection with Fe³⁺ beam. A rotating energy degrader foil was applied for obtaining a rather homogenous distribution of helium atoms in specimens. The fluxes of He⁺ and Fe³⁺ ion beams were approximately 1.5×10^{16} ions m⁻² s⁻¹, 1.7×10^{16} ions m⁻² s⁻¹, respectively. The irradiation temperature was measured by an infrared thermography to be 550 °C within a fluctuation of ±10 °C. All three types of ODS steels were irradiated together for about 8 h.

The injected helium concentration and displacement damage (displacements per atom, dpa) were obtained by SRIM [36] simu-

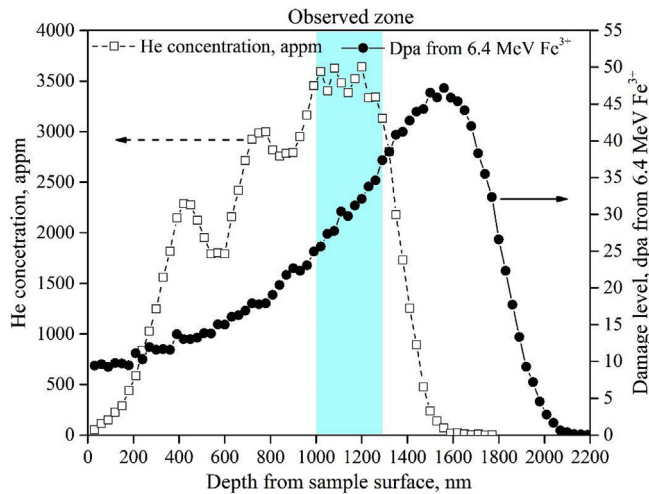


Fig. 1. SRIM simulation results of damage level, dpa and He concentration, appm.

lation, and shown in Fig. 1. The nominal displacement damage at 600 nm depth was 15 dpa, and in the depth range from 1000 to 1300 nm, the damage level and helium concentration were approximately 30 dpa and 3500 appm, respectively.

2.3. Transmission electron microscopy (TEM)

Cross-sectional TEM specimens were prepared by using the FIB lift-out technique, followed by the flash polishing with 5% (vol.) HClO_4 and 95% (vol.) CH_3OH around -35°C to remove a FIB damage layer. Dislocations and oxide particles were imaged under kinematical bright field (KBF) image conditions ($\mathbf{g} = \langle 110 \rangle$, $\mathbf{s}_g \neq 0$) by using a conventional 200 kV JEOL JEM 2010 microscope. Meanwhile, helium bubbles were imaged by Fresnel contrast at both under- and over-focused conditions. The thickness of the observation area in TEM foil was obtained by measuring the fringe spacing in Convergent Beam Electron Diffraction (CBED) patterns.

2.4. Hardness measurements

Vickers hardness was measured for as-received ODS bulk samples using a diamond indenter with a Vickers hardness tester (HMV-G21, Shimadzu). The sample surface tested was perpendicular to the extrusion direction. The load and dwell time were 1 kg and 10 s, respectively. 10 tests were done for each sample and the averaged values were obtained.

Nanoindentation testing was performed on as-received and irradiated samples by using a nanoindenter (Agilent G200) equipped with a Berkovich tip. A continuous stiffness measurement (CSM) was adopted to obtain continuous hardness and elastic modulus as a function of indentation depth. Before testing, the indenter tip geometry was calibrated by indenting a fused silica reference sample with known mechanical properties. Other main testing parameters were depicted as follows: the maximum indentation depth was 2000 nm, the strain rate was 0.05 s^{-1} , the harmonic displacement was 1 nm, and the Poisson's ratio was 0.3. For each specimen, 24 testing points (60 μm between two adjacent points) were chosen and the averaged hardness was obtained by calculating the measured hardness data of roughly 20 tests after several test results were omitted because of the significance in the data scattering.

3. Results and discussion

3.1. TEM examinations

3.1.1. Microstructure before irradiation

Prior to irradiation, oxide particles and dislocation structures of Y-Al-ODS were observed under KBF image contrast by using $\mathbf{g} = [1-10]$ close to zone $[111]$, and shown in Fig. 2(a) with the corresponding particle size distribution in Fig. 2(b). The related dispersion parameters of oxide particles for the three ODS ferritic steels were summarized in Table 1. The average particle spacing distance (λ_o) was calculated as $[(N_o)^{-1/3} - d_o]$, where N_o and d_o were the particle number density and the mean diameter, respectively [37]. The dislocation densities in as-received ODS ferritic steels are presented in Table 2. Grains were found to be elongated parallel to the extrusion direction and the grain size of Y-Al-ODS was measured to be about 0.46 μm in width based on the STEM bright-field image.

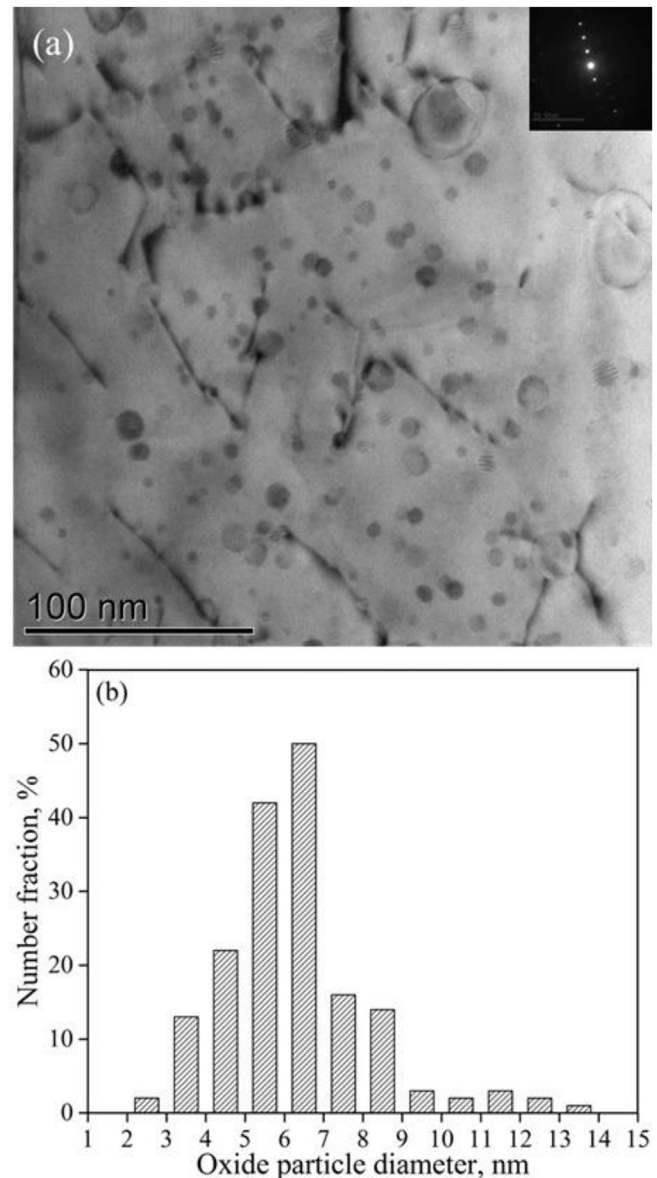


Fig. 2. (a) oxide particles and dislocations in as-received Y-Al-ODS steel and (b) the corresponding particle size distribution.

Table 1

Mean diameter (d_o), number density (N_o), volume fraction (f_o) and averaged distance (λ_o) of oxide particles in the three as-received ODS ferritic steels.

	Y-Ti-ODS [19]	Y-Al-ODS	Y-Al-Zr-ODS [19]
d_o , nm	3.0 ± 0.1	6.3 ± 0.2	6.2 ± 0.1
N_o , m^{-3}	$(1.1 \pm 0.1) \times 10^{23}$	$(1.9 \pm 0.1) \times 10^{22}$	$(3.5 \pm 0.6) \times 10^{22}$
f_o , %	0.18 ± 0.02	0.32 ± 0.03	0.52 ± 0.08
λ_o , nm	17.6 ± 0.1	31.2 ± 0.2	24.3 ± 0.1

Table 2

Dislocation density (ρ) in the depth range of 1000–1300 nm (~30 dpa) in the three ODS steels before and after ion irradiation.

ρ , $\times 10^{14} m^{-2}$	Y-Ti-ODS	Y-Al-ODS	Y-Al-Zr-ODS
As-received	1.2 [19]	1.2	1.4 [19]
Single beam	1.1	0.7	2.1
Dual beam	0.3	1.1	2.8

3.1.2. Ion-irradiation induced He bubbles and dislocations

Fig. 3 shows a TEM cross-sectional micrograph of whole range of the damage layer in Y-Al-ODS irradiated with dual ion beams where numerous tiny bubbles were mainly distributed in the depth region of 600–1600 nm. The distribution of helium bubbles after dual ion beam irradiation was well consistent with the SRIM simulation results, while in the case of single ion beam irradiation, tiny voids with negligible number densities were observed.

In order to distinguish between the contrasts of helium bubbles and oxide particles to accurately investigate the positional relationship between the two, helium bubbles were observed with Fresnel contrast technique at under to over focused conditions with KBF imaging using $g = \langle 110 \rangle$. The distribution of both helium bubbles and oxide particles after the dual ion irradiation are shown in Fig. 4(a)–4(c) for Y-Ti-ODS, Fig. 4(d)–4(f) for Y-Al-ODS and Fig. 4(g)–4(i) for Y-Al-Zr-ODS steel in the region from 1000 to

1300 nm depth with approximately 30 dpa and 3500 appm He concentration. Helium bubbles, oxide particles as well as dislocations were characterized for each ODS steel. The bright spots in the under focused images (Fig. 4(a) and 4(d) and 4(g)) became dark spots in the over-focused images (Fig. 4(c) and 4(f) and 4(i)), from which it could be judged that the spots corresponded to helium bubbles. The black spots in in-focused images (Fig. 4(b) and 4(e) and 4(h)) were mostly oxide particles and the other precipitates. Precise TEM observations revealed that most of the imaged helium bubbles nucleated as attached to oxide particles by side to side, which was further verified in this research with the use of high resolution STEM BF imaging conditions for dual beam irradiated Y-Al-ODS. The numerical data of the mean diameter and the number density of helium bubbles were obtained by counting 610 helium bubbles in TEM photos and given in Table 3. Smaller the helium bubbles tended to increase the number density. The reason for the distribution difference of helium bubbles among the three ODS steels is discussed in the next section. The fraction of helium bubbles affiliated with oxide particles were estimated to be 73.7%, 81.4% and 82.2% for Y-Ti-ODS, Y-Al-ODS and Y-Al-Zr-ODS, respectively. These values might be overestimated essentially due to invisible dislocations, oversight of helium bubbles formed at grain boundaries and unavoidable overlay in a two-dimensional micrograph. C.M. Parish et al. estimated the fraction of bubbles associated with precipitates to be roughly 40% by virtue of STEM chemical analysis after dual ion (Fe, He) beam irradiation up to ~20 dpa and ~450–750 appm He implantation at 650 °C [10]. Although the trapping capacity appears to depend on the oxide particles and/or precipitates, it is clear that the oxide/matrix interfaces can effectively trap helium atoms, accelerating the formation of more stable helium bubbles adjacent to oxide particles [38].

In our previous research, single He⁺ implantation to ~3500 appm He/0.2 dpa at 550 °C [19] resulted in a similar helium bubbles distribution with a mean diameter and number density of 2.5 ± 0.1 nm, $(1.6 \pm 0.4) \times 10^{23} m^{-3}$ and 5.0 ± 0.5 nm,

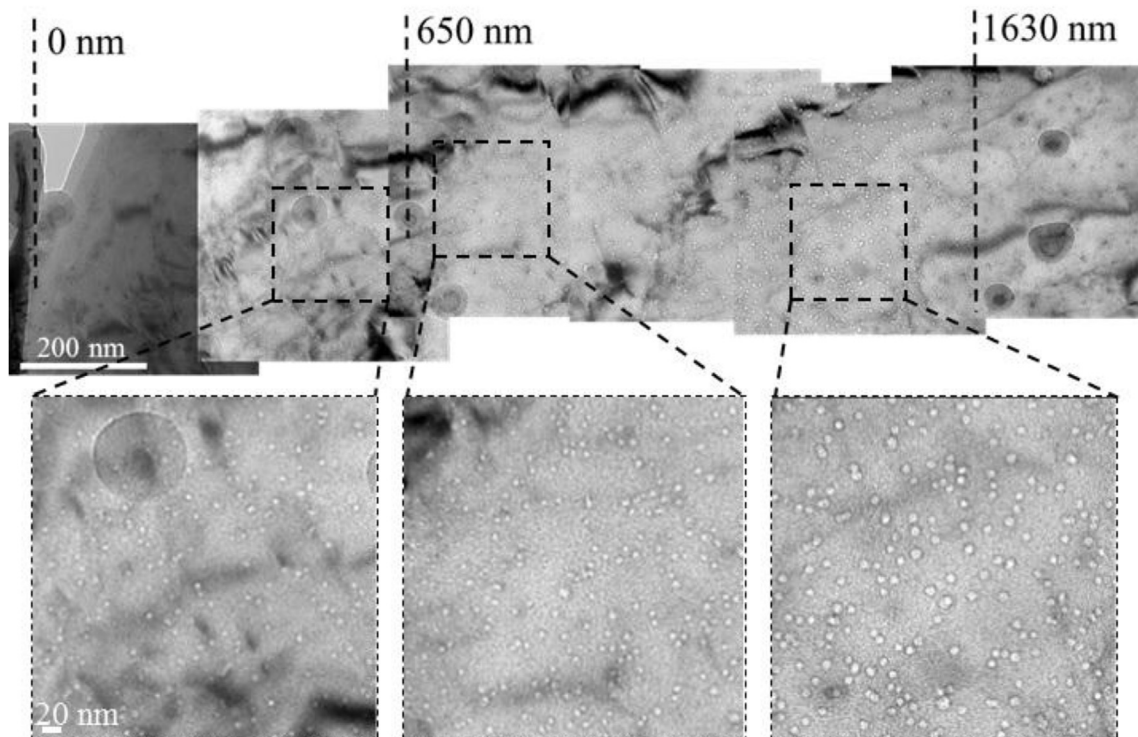


Fig. 3. He bubble distribution in Y-Al-ODS steel after dual-beam irradiation.

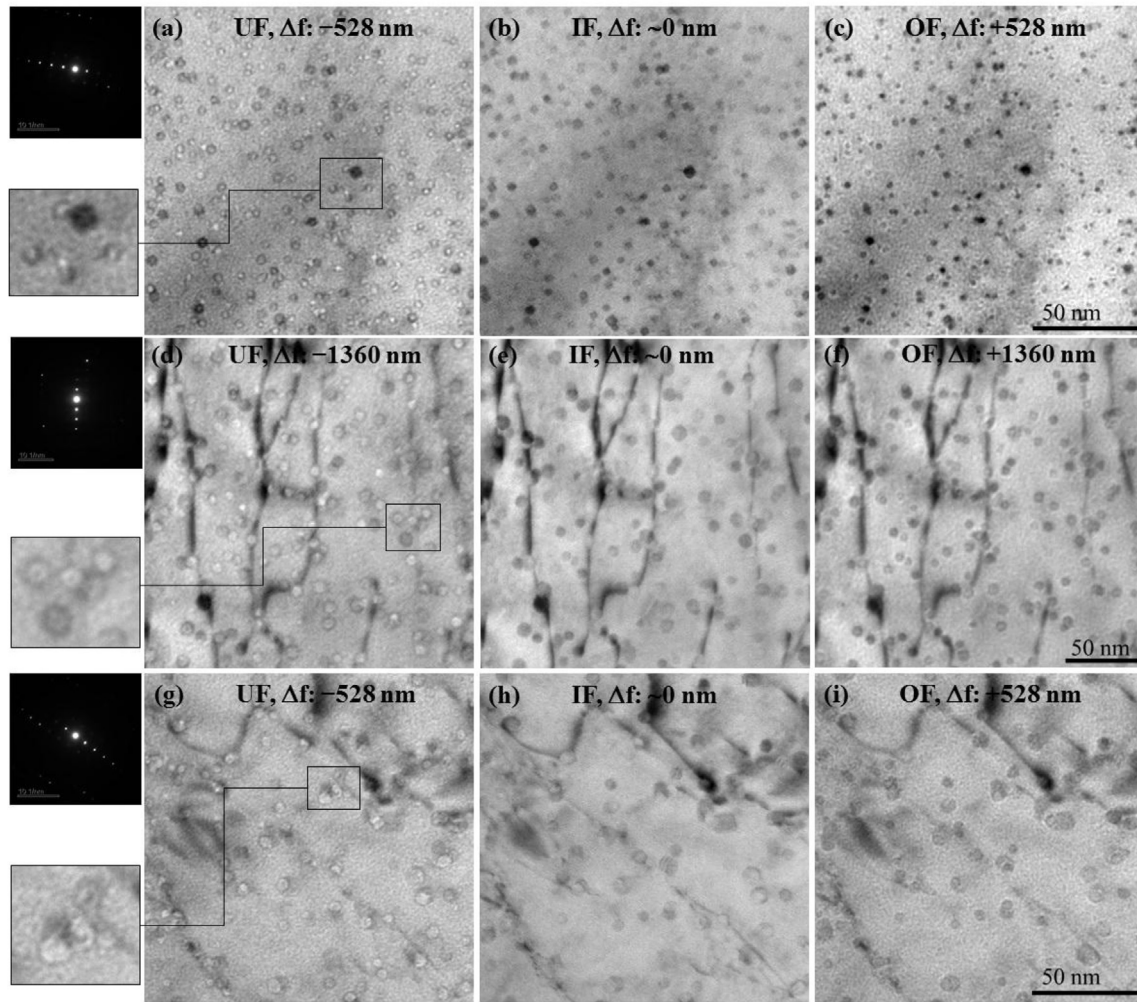


Fig. 4. TEM observations of He bubbles, oxide particles and dislocation lines in Y-Ti-ODS (a–c), Y-Al-ODS (d–f), Y-Al-Zr-ODS (g–i) with changing focus conditions from under-focus to over-focus; a nominal damage of approximately 30 dpa and He concentration of 3500 appm. The farthest left magnified images show He bubbles attached to oxide particles. All images were taken by using $g = [110]$ close to pole $[001]$; the diffraction pattern for the TEM images located in the same column. UF: under focus, IF: in focus, OF: over focus.

Table 3

Mean diameter (d_b), number density (N_b) of He bubbles, swelling ($\Delta V/V$), the number (T) of counted bubbles and the fraction (F) of bubbles adjacent to oxide particles in the depth range of 1000–1300 nm under dual beam irradiation.

	Y-Ti-ODS	Y-Al-ODS	Y-Al-Zr-ODS
d_b , nm	2.8 ± 0.1	6.6 ± 1.0	4.5 ± 0.2
N_b , m^{-3}	$(1.1 \pm 0.1) \times 10^{23}$	$(2.7 \pm 0.2) \times 10^{22}$	$(3.6 \pm 0.6) \times 10^{22}$
$\Delta V/V$, %	0.13 ± 0.02	0.53 ± 0.19	0.20 ± 0.04
T ; F , %	287; 73.7	194; 81.4	129; 82.2

$(5.2 \pm 0.2) \times 10^{22} m^{-3}$ for Y-Ti-ODS and Y-Al-Zr-ODS, respectively, which suggests that the two orders of magnitude of difference in the He/dpa ratio never causes a significant effect on the He bubble formation. At high temperatures between $0.2T_m$ and $0.5T_m$ (T_m : the melting temperature), not the damage rate but the flux of He^+ implantation can effectively stabilize helium-vacancy clusters above some critical sizes [39]. As a result, bubble embryos were nucleated at a higher number density irrespective of damage rate.

Dislocations were observed using $g = \langle 110 \rangle$ for three ODS steels irradiated with dual (Fe^{3+} and He^+) beam and single Fe^{3+} beam irradiation. The measured line dislocation densities in the three steels are shown in Table 2, and an example of dislocation segments is shown in Fig. 5 for Fe^{3+} irradiated Y-Ti-ODS. After irradiation, the

line dislocation density appeared to decrease in Y-Ti-ODS and Y-Al-ODS, although some dislocations were invisible due to the $g \cdot b = 0$ condition. No dislocation loops were found at this irradiation temperature (550 °C). This result was consistent with the other ODS steels irradiated with single Fe ion beam at 500 °C [40] and dual (Fe-ion and He-ion) beam at 650 °C [41], while in the neutron irradiated ODS ferritic alloy at 500 °C, dislocation loops with two sorts of Burgers vectors, $a/2\langle 111 \rangle$ and $a\langle 100 \rangle$, were observed [13]. This difference is considered to be attributed to high dpa rate in heavy-ion irradiations ($\sim 1.0 \times 10^{-3}$ dpa/s in this research), providing effective spatial overlap of cascades above about 0.01 dpa [42]. Consequently, the majority of radiation induced defects can be annihilated by mutual recombination of one vacancy/vacancies and one interstitial/interstitials especially at elevated temperatures.

3.1.3. Swelling

The void swelling calculated on the basis of bubble size distribution [43] was estimated to be 0.13%, 0.53% and 0.20% in Y-Ti-ODS, Y-Al-ODS and Y-Al-Zr-ODS, respectively. The difference in swelling can be explained in terms of trapping capacity at oxide particles, dislocations and grain boundaries. According to the previous study [3], the sink strength is described by the number of trapping sites per unit area, where the sink strength of dislocations, Z_d , is denoted

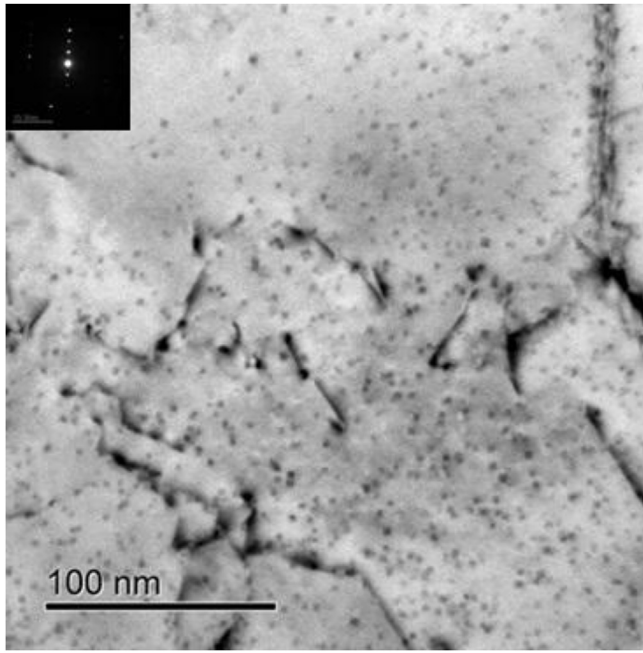


Fig. 5. Microstructures in single (Fe^{2+}) beam irradiated Y-Ti-ODS with a nominal damage of 30 dpa, imaged by using $\mathbf{g} = [1\bar{1}0]$ close to pole $[110]$ under KBF.

by the dislocation density, while the sink strength of oxide particles, Z_o , is expressed by $2\pi N_o d_o$, where N_o and d_o are the mean diameter and the number density of oxide particles, respectively. And the sink strength of grain boundaries, Z_{gb} , is given by $15/h^2$, where h is the average grain size [44]. Here, the average grain sizes of Y-Ti-ODS and Y-Al-Zr-ODS were around 370 nm [19] and that of Y-Al-ODS was roughly 460 nm. The calculated sink strength values are summarized in Table 4. It turns out that the oxide particles act as dominant sinks for defect recombination and/or bubble nucleation when compared to dislocations and grain boundaries. Nevertheless, the heterogeneous distribution of helium bubbles may be caused by the sparse distribution of oxide particles and dislocations in grains. Under these circumstances, numerous intergranular bubbles were formed (see Fig. 6), demonstrating the strong sinking effects of grain boundaries.

Actually, $\text{He}_n\text{-V}_m$ ($n = 1, 2, 3$ and $m = 0, 1$) clusters have much lower formation energies at the ferrite/ $\text{Y}_2\text{Ti}_2\text{O}_7$ interfaces than in the ferrite matrix [45], implying the preferential nucleation of a helium bubble nucleus at oxide/matrix interfaces. A short distance between neighboring oxide particles can enhance the trapping probability of helium, point defects and their clusters, which leads to the formation of helium bubbles in a high number density at the oxide particles. Once a helium bubble is formed, the bubble does immediately behave as an excellent sink for point defects [3] and further improves the swelling resistance of ODS steels. An increased number density of bubbles in Y-Ti-ODS compared to the

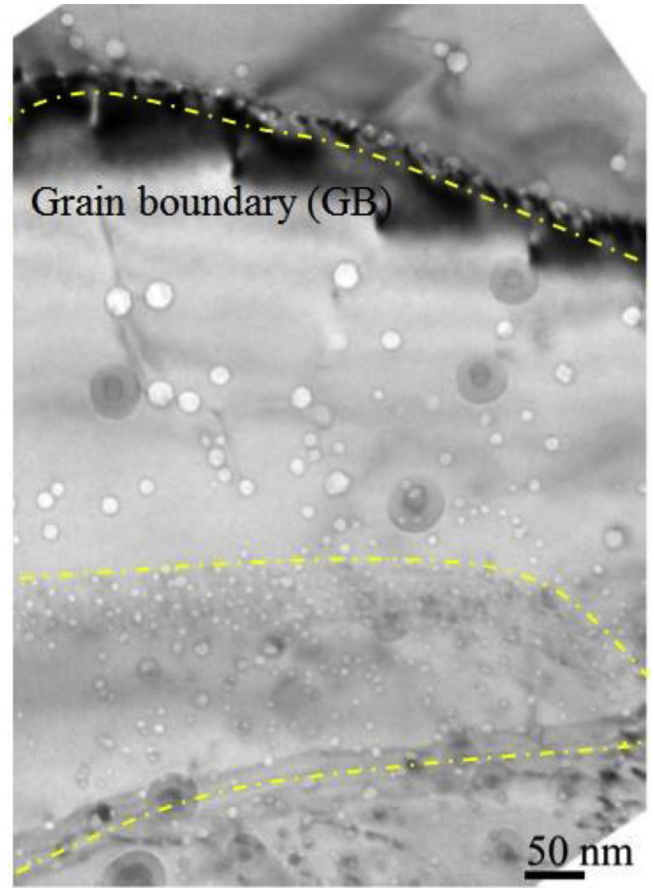


Fig. 6. Inhomogeneous He bubble distribution in dual beam irradiated Y-Al-ODS steel. GB is marked by three dash lines.

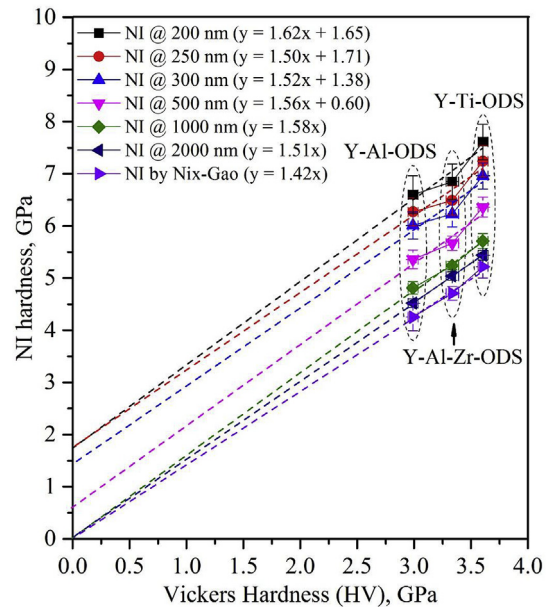


Fig. 7. Nanoindentation (NI) hardness at different indentation depths and obtained by the Nix-Gao model as a function of Vickers hardness (HV) for the three as-received ODS steels.

Table 4

Estimated sink strengths of oxide particles (Z_o), line dislocations (Z_d) and grain boundaries (Z_{gb}) on the assumption that a lattice site provides a trapping site.

($\times 10^{14} \text{ m}^{-2}$)	Y-Ti-ODS [19]	Y-Al-ODS	Y-Al-Zr-ODS [19]
Z_o	20.7	7.5	13.6
Z_d	0.3	1.1	2.8
Z_{gb}	1.1	0.7	1.1

^a Sink strengths of line dislocation come from that of the ODS specimens after dual beam irradiation.

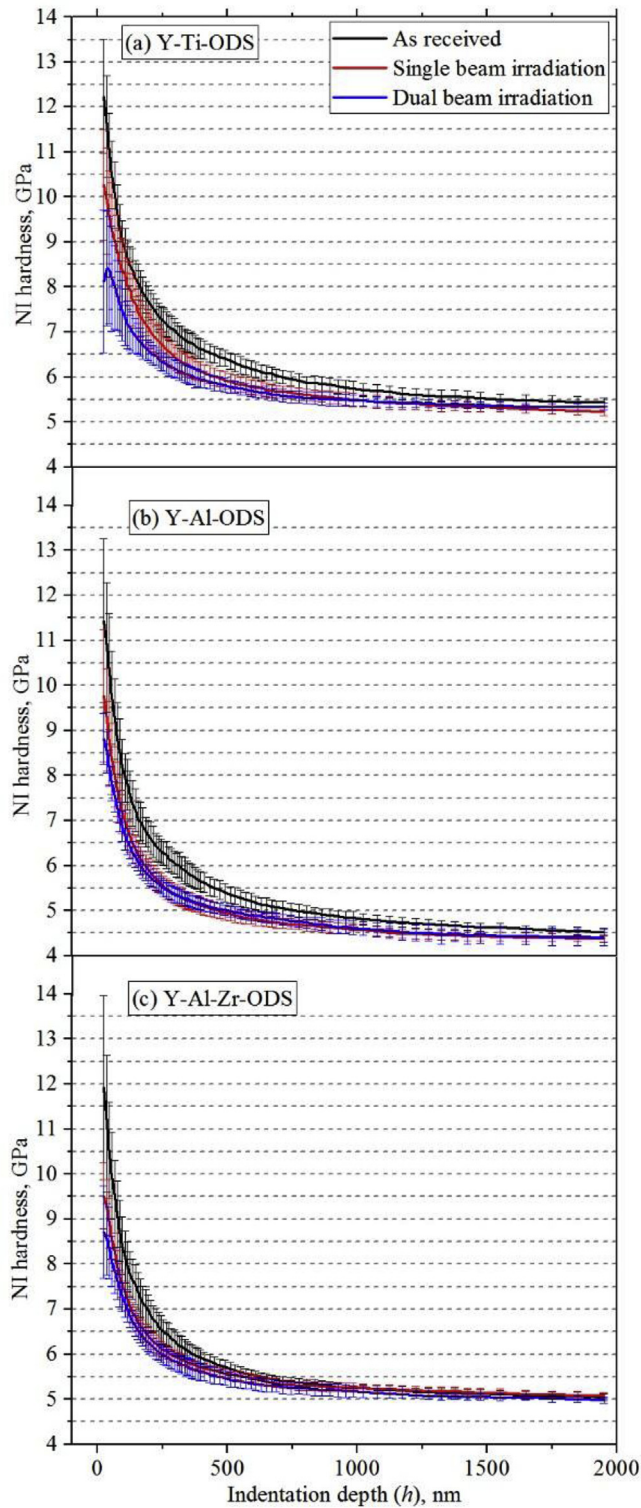


Fig. 8. Averaged depth profiles of nanoindentation (NI) hardness of (a) Y-Ti-ODS, (b) Y-Al-ODS and (c) Y-Al-Zr-ODS: black/unirradiated, red/single ion irradiated, blue/dual ion irradiated (color figure). (For interpretation of the references to color in this figure legend, the reader is referred to the Web version of this article.)

Y-Al-ODS and Y-Al-Zr-ODS alloys was mainly attributed to the higher number density of oxide particles in Y-Ti-ODS.

As discussed before in this section, the sink strength is a measure of the number of trapping sites per unit area, and the

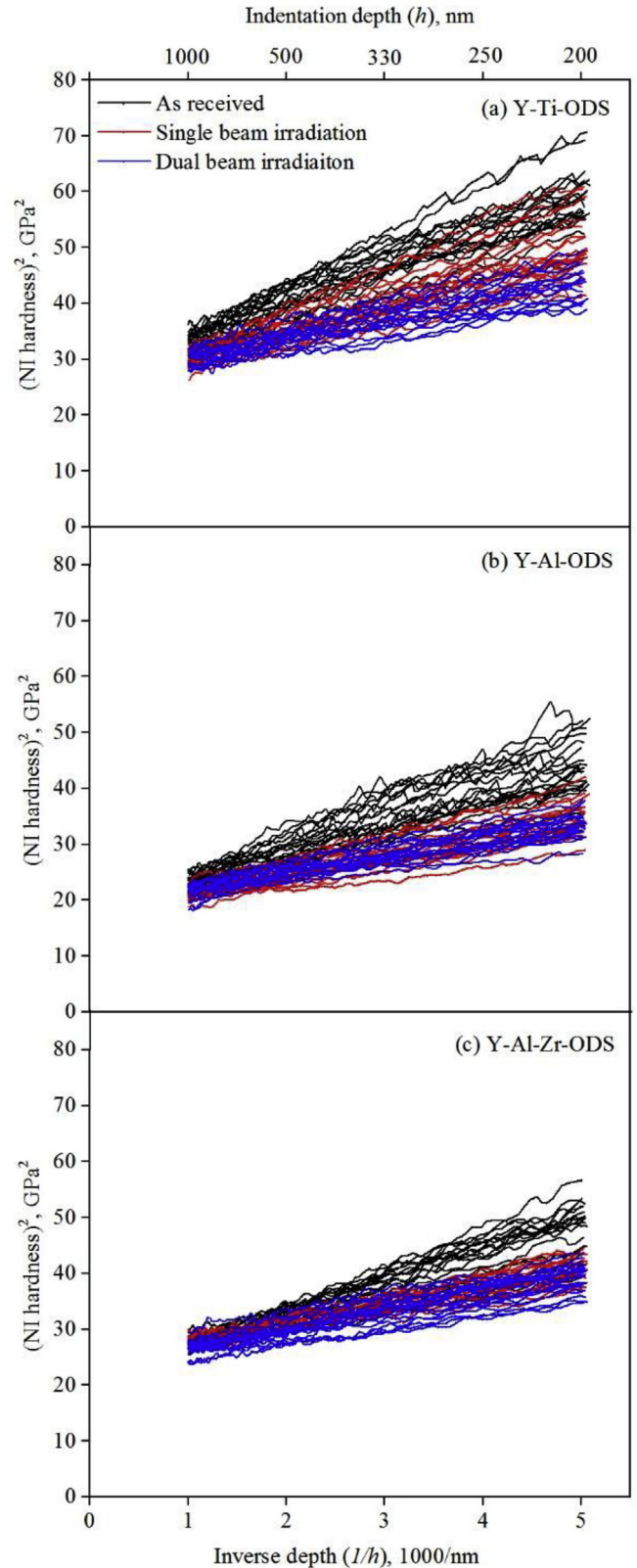


Fig. 9. H^2 versus $1/h$ plots of all nanoindentation (NI) hardness data based on the Nix-Gao model for (a) Y-Ti-ODS, (b) Y-Al-ODS and (c) Y-Al-Zr-ODS: black/unirradiated, red/single ion irradiated, blue/dual ion irradiated (color figure).

difference in the swelling among the three ODS steels was well explained by the sink strength estimated from the TEM

examinations. A similar trend was also observed in other research on ODS steels containing one type of oxide particle [18,44]. However, at a very high He concentration, trapping efficiency, which is the number of helium atoms trapped at a site, should be taken into account and it can be changed among different types of oxide particles since it might be determined by the binding energy between the helium atom and the trapping site. A simulation study is effective to discuss this issue and to clarify the effect of type of oxide particles which have different crystal structures as observed in Y-Ti-ODS [46], Y-Al-ODS [32] and Y-Al-Zr-ODS [33].

3.2. Hardness measurements

3.2.1. Hardness before irradiation

Fig. 7 shows the relationship between Vickers hardness (H_V) and nanoindentation (NI) hardness of as-received ODS steels. The NI hardness was obtained by two methods: one is by obtaining the values at each indentation depth of 200, 250, 300, 500, 1000 and 2000 nm in the depth profile of NI (see the averaged black lines in Fig. 8(a) and 8(b) and 8(c)), and the other is by applying the Nix-Gao model to all of the measured data of the indentation depth from 200 to 1000 nm (see black lines in Fig. 9(a) and 9(b) and 9(c)) [47].

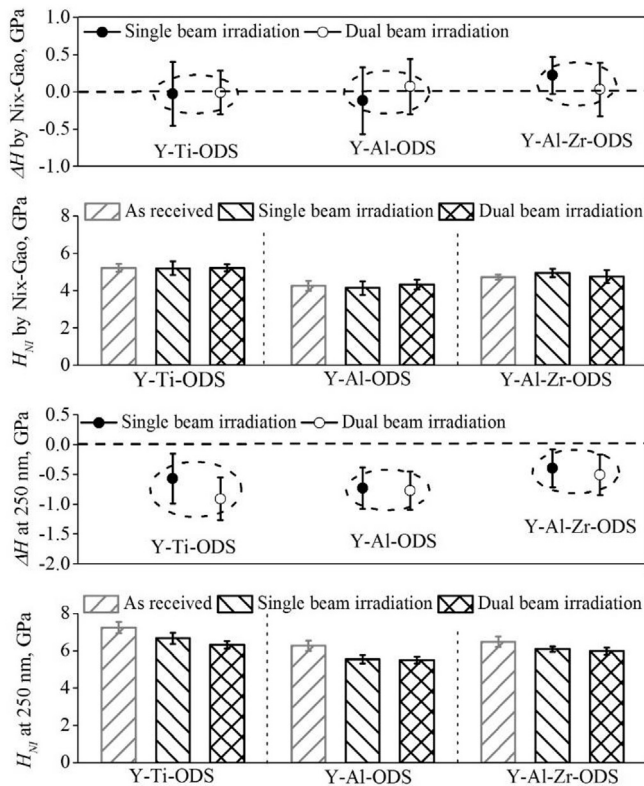


Fig. 10. Nanoindentation (NI) hardness (H_{NI}) and the corresponding hardness changes (ΔH_{NI}) at the indentation depth of around 250 nm and that obtained by applying the Nix-Gao model to each H^2 versus $1/h$ plot.

Table 5

Nanoindentation (NI) hardness at the indentation depth of around 250 nm and obtained by the application of the Nix-Gao model before and after ion-irradiation.

(GPa)	Y-Ti-ODS			Y-Al-ODS			Y-Al-Zr-ODS		
	As received	Single	Dual	As received	Single	Dual	As received	Single	Dual
NI hardness @ 250 nm	7.24 ± 0.30	6.67 ± 0.30	6.33 ± 0.20	6.27 ± 0.27	5.54 ± 0.22	5.50 ± 0.18	6.49 ± 0.28	6.09 ± 0.15	5.98 ± 0.19
NI hardness by Nix-Gao	5.22 ± 0.22	5.19 ± 0.37	5.21 ± 0.19	4.25 ± 0.26	4.13 ± 0.37	4.32 ± 0.26	4.72 ± 0.13	4.94 ± 0.22	4.75 ± 0.34

As shown in Fig. 8, in the near surface region, below the depth of 50 nm, NI hardness increased abruptly with increasing depth, which is known as the reverse indentation size effect (ISE) and is often ascribed to testing artifacts [48]. In the depth range of deeper than 50 nm, a normal ISE was observed where the hardness decreased with increasing indentation depth, which is considered to be due to so called geometrically necessary dislocations (GND) that mathematically decreases dislocation density with increasing indentation depth [48].

Fig. 7 shows that there is a proportional relationship between the Vickers hardness and the NI hardness obtained by the Nix-Gao model and the NI hardness obtained at 1000 and 2000 nm, in both of which the indentation size effect (ISE) can be neglected. Meanwhile a linear relationship can be seen for the NI hardness obtained at 200, 250, 300 and 500 nm, where the ISE became significant. It is considered that the intercept values of the lines of the linear equations reflect the amount of GND of ISE.

Generally, it can be said that the NI hardness is expressed as $H_{NI} = 1.5H_V$. The mismatch between H_V and H_{NI} is considered to be due to the difference in the hardness measurement technique between the two methods. As for the NI hardness value obtained at each indentation depth, it becomes larger with smaller indentation depth, which is known as ISE. Although the NI hardness was roughly 1.5 times larger than the Vickers hardness, there was a good correlation in the order of the hardness: Y-Ti-ODS > Y-Al-Zr-ODS > Y-Al-ODS. The strengthening mechanisms were discussed in Ref. [49].

3.2.2. Irradiation induced hardness changes

As explained in the previous section, the NI hardness after ion-irradiation was analyzed by two methods: one is the conventional method to measure the NI hardness at a constant indentation depth and the other is to measure the hardness following the Nix-Gao model. In the former, the hardness at the indentation depth of 250 nm was measured for three ODS ferritic steels before and after irradiation. In fact, the plastic zone at the 250 nm indentation depth was reported to be able to reflect the hardness of the peak damage region (approximately 1600 nm) at the present ion-irradiation experimental conditions [50]. In the latter, NI hardness was extrapolated by applying the Nix-Gao model to each H^2 versus $1/h$ plot of the irradiated specimens in the indentation depth range from around 200 to 250 nm, as shown in Fig. 9(a) and 9(b) and 9(c). All hardness values obtained by the above two methods were shown in Fig. 10 and the numerical values are summarized in Table 5.

The NI hardness derived by the former indicated that the three ODS ferritic steels were softened by both single Fe^{3+} and dual (Fe^{3+} and He^+) beam irradiation. The softening was rather evident in dual beam irradiated Y-Ti-ODS (-0.91 ± 0.36 GPa at 250 nm) and Y-Al-ODS (-0.77 ± 0.32 GPa at 250 nm). Such phenomenon was also found in reduced activation martensitic steels under neutron irradiation at temperatures above 423 °C which is much lower than the threshold temperature of 600 °C beyond which the martensite phase became unstable [51,52]. The softening behavior might be owing to the radiation enhanced recovery of dislocation structures.

However, a different trend showing no significant ion irradiation hardening was found in the NI hardness measured by the Nix-Gao model. This result is consistent with a hardness decreasing significantly as the irradiation temperature increases to 500 °C in single He⁺ or Fe³⁺ irradiated ODS steels [22,40].

3.3. Correlation between microstructure and hardness

In this study, ion-irradiation induced the changes in dislocation density and in the distribution morphology of vacancy clusters. The contribution of dislocations to hardness is estimated by the following equation [43]:

$$\Delta\sigma_d = M\alpha_d\mu\Delta\rho^{0.5} \quad (1)$$

where $\Delta\sigma_d$ is the change in the tensile yield stress; M is the Taylor factor (3.06); α_d is the strength factor of line dislocations, equal to 0.212 [50]; μ is the shear modulus (80 GPa for alpha iron); b is the Burgers vector (0.248 nm for 1/2<111> dislocations in alpha iron); $\Delta\rho^{0.5}$ is the change in the square root of dislocation density obtained by TEM measurements. Meanwhile, the tensile yield stress can be converted to Vickers hardness following the relationship, $\Delta\sigma$ (MPa) = 0.3 ΔHV (MPa) [53]. Softening induced by the reduction of the dislocation density only occurred in dual beam irradiated Y-Ti-ODS and Fe beam irradiated Y-Al-ODS, estimated as $\Delta H = -0.35$ GPa (−348 MPa) and -0.16 GPa (−162 MPa), respectively, smaller than the corresponding values $\Delta H_{NI} = -0.91 \pm 0.36$ GPa and -0.73 ± 0.35 GPa measured by the conventional method (at 250 nm) in NI tests. It is possible that the reduction of the dislocation density after ion irradiations can be underestimated due to the inhomogeneous distribution of dislocations in ODS steels and the $\mathbf{g} \cdot \mathbf{b} = 0$ invisibility criteria, but it can be still concluded that the contribution of the difference in the density of line dislocations to hardness is negligible. Taking the NI hardness results into account, we can conclude that no hardening was induced by ion irradiation at 550 °C in the studied ODS steels irradiated with single ion or dual ions.

According to the TEM observation results, another possible contribution to hardening might be He bubbles, which is calculated by the Orowan hardening model $\Delta\sigma_b = M\alpha_b\mu b(N_b d_b)^{0.5}$, where N_b and d_b are the number density and mean diameter of He bubbles, respectively [43]. In the present study, the hardening by voids or bubbles can be ignored regarding the NI hardness results and no significant dislocation recovery, although there are several studies showing a rather large contribution of voids or bubbles to irradiation hardening with a strength factor α_b of 0.3–0.6 estimated from experimental results [54,55] and 0.2–0.4 obtained through molecular dynamics (MD) simulations on cavities in the diameter range of 1–4 nm [7].

It is considered that voids and helium bubbles with high He content may be short-range obstacles for dislocation motion [43,56] and helium bubbles at grain boundaries (GB) cause intergranular embrittlement [39,43,57]. Therefore helium may degrade fracture toughness by different mechanisms: hardening mechanism, non-hardening (GB embrittlement) mechanism and their synergistic effect. Previous research on helium effects showed that a significant amount of irradiation hardening remained after post-irradiation annealing at temperatures between 550 and 600 °C in neutron irradiated RAFM steels up to 11.3 dpa/1175 appm He [29] and in helium implanted reduced activation martensitic steel up to 0.2 dpa/580 appm He [23]. The residual hardening was attributed to helium bubbles which still survived the annealing process. Detailed TEM examinations, however, are necessary to prove the annealing effects on the hardness.

In this research, the insignificant bubble hardening may be

relevant to the great fractions of helium bubbles adjacent to oxide particles (from about 74% to 82%). Because of the identical position of helium bubbles and oxide particles, the number density of obstacles to dislocation motion doesn't change by the formation of helium bubbles, known as "strength superposition effect". Based on this effect, the negligible contribution of isolated He bubbles (around 20%) from oxide particles to hardening allows the strength factor α_b to be 0.1–0.2. Besides, it is expected that there is a critical helium concentration that exceeds the upper limit of helium trapping capacity in ODS steels as also proposed for conventional ferritic/martensitic steels [39].

4. Conclusions

Helium bubble formation behavior, swelling and hardness changes were investigated for three ion irradiated ODS ferritic steels (Y-Ti-ODS, Y-Al-ODS and Y-Al-Zr-ODS), which were strengthened by different types of oxide particles. Single Fe³⁺ and dual (Fe³⁺ and He⁺) beam irradiations were performed at 550 °C with a damage of around 30 dpa and helium concentration of 3500 appm in the depth range of 1000–1300 nm. The main results are as follows:

- 1). Three ODS steels possessed similar grain sizes (370 nm for Y-Ti-ODS and Y-Al-Zr-ODS, 460 nm for Y-Al-ODS) and dislocation densities ($\sim 10^{14} \text{ m}^{-2}$). The mean diameters and number densities of oxide particles were 3.0 nm/ $1.1 \times 10^{23} \text{ m}^{-3}$, 6.3 nm/ $1.9 \times 10^{22} \text{ m}^{-3}$ and 6.2 nm/ $3.5 \times 10^{22} \text{ m}^{-3}$ for Y-Ti-ODS, Y-Al-ODS and Y-Al-Zr-ODS, respectively.
- 2). After dual-beam irradiation, nano-sized helium bubbles were observed. The mean diameter and the number density of helium bubbles were 2.8 nm/ $1.1 \times 10^{23} \text{ m}^{-3}$, 6.6 nm/ $2.7 \times 10^{22} \text{ m}^{-3}$ and 4.5 nm/ $3.6 \times 10^{22} \text{ m}^{-3}$ in Y-Ti-ODS, Y-Al-ODS and Y-Al-Zr-ODS, respectively. About 80% of the intragranular helium bubbles were adjacent to oxide particles in the three ODS ferritic steels.
- 3). Void swelling in Y-Ti-ODS, Y-Al-ODS and Y-Al-Zr-ODS was 0.13%, 0.53% and 0.20%, respectively, in accordance with the total sink strength estimated by counting the number of trapping sites. It is considered that the morphology of oxide particle dispersion not the oxide particle/matrix (O/M) interface structure was the main contributor for suppressing swelling in despite of different crystal structures of dominant oxide particles in the three ODS steels.
- 4). No dislocation loops were found in the three ODS steels after ion-irradiation at 550 °C irrespective of helium implantation.
- 5). No hardening was observed in the three ODS steels irradiated with both single Fe³⁺ and dual (Fe³⁺ and He⁺) ions and the possible softening should be considered to be due to radiation enhanced recovery of dislocations. The comparison between hardness values of the three ODS steels after single and dual beam irradiation provided evidence that a high number density of helium bubbles caused negligible hardening, which should be related to the results that the majority of helium bubbles formed were adjacent to oxide particles in the three ODS steels.

Acknowledgments

The first author wishes to acknowledge Japanese Government (MEXT) for scholarship and the China Scholarship Council for their kind support. The authors are also grateful to the technical support by members of Application of Duet and Muster for Industrial Research and Engineering (ADMIRE), Kyoto University.

References

- [1] A. Kimura, R. Kasada, N. Iwata, et al., Development of Al added high-Cr ODS steels for fuel cladding of next generation nuclear systems, *J. Nucl. Mater.* 417 (2011) 176–179.
- [2] S. Ukai, M. Fujiwara, Perspective of ODS alloys application in nuclear environments, *J. Nucl. Mater.* 307–311 (2002) 749–757.
- [3] G.R. Odette, M.J. Alinger, B.D. Wirth, Recent developments in irradiation-resistant steels, *Annu. Rev. Mater. Res.* 38 (2008) 471–503.
- [4] S.J. Zinkle, L.L. Snead, Designing radiation resistance in materials for fusion energy, *Annu. Rev. Mater. Res.* 44 (2014) 241–267.
- [5] A. Kimura, H. Cho, N. Toda, et al., High burnup fuel cladding materials R&D for advanced nuclear systems, *J. Nucl. Sci. Technol.* 44 (2007) 323–328.
- [6] B.A. Pint, K.A. Unocic, K.A. Terrani, Effect of steam on high temperature oxidation behavior of alumina-forming alloys, *Mater. High. Temp.* 32 (2015) 28–35.
- [7] Y. Dai, G.R. Odette, T. Yamamoto, The Effects of Helium in Irradiated Structural Alloys, *Comprehensive Nuclear Materials*, Elsevier, Amsterdam, 2012, pp. 142–189.
- [8] G.R. Odette, P. Miao, D.J. Edwards, et al., Helium transport, fate and management in nanostructured ferritic alloys: In situ helium implantation studies, *J. Nucl. Mater.* 417 (2011) 1001–1004.
- [9] C.M. Parish, M.K. Miller, Aberration-corrected X-ray spectrum imaging and Fresnel contrast to differentiate nanoclusters and cavities in helium-irradiated alloys 14YWT, *Microsc. Microanal.* 20 (2014) 613–626.
- [10] C.M. Parish, K.A. Unocic, L. Tan, et al., Helium sequestration at nanoparticle-matrix interfaces in helium + heavy ion irradiated nanostructured ferritic alloys, *J. Nucl. Mater.* 483 (2017) 21–34.
- [11] Q. Li, C.M. Parish, K.A. Powers, et al., Helium solubility and bubble formation in a nanostructured ferritic alloy, *J. Nucl. Mater.* 445 (2014) 165–174.
- [12] G.R. Odette, Recent progress in developing and qualifying nanostructured ferritic alloys for advanced fission and fusion applications, *JOM* 66 (2014) 2427–2441.
- [13] H.J. Jung, D.J. Edwards, R.J. Kurtz, et al., Structural and chemical evolution in neutron irradiated and helium-injected ferritic ODS PM2000 alloy, *J. Nucl. Mater.* 484 (2017) 68–80.
- [14] P. Erhart, A first-principles study of helium storage in oxides and at oxide-iron interfaces, *J. Appl. Phys.* 111 (2012) 113502.
- [15] Y. Jin, Y. Jiang, L. Yang, et al., First principles assessment of helium trapping in Y_2TiO_5 in nano-featured ferritic alloys, *Appl. Phys.* 116 (2012) 143501.
- [16] T. Yamamoto, Y. Wu, G.R. Odette, et al., A dual ion irradiation study of helium-dpa interactions on cavity evolution in tempered martensitic steels and nanostructured ferritic alloys, *J. Nucl. Mater.* 449 (2014) 190–199.
- [17] K. Yutani, H. Kishimoto, R. Kasada, et al., Evaluation of helium effects on swelling behavior of oxide dispersion strengthened ferritic steels under ion irradiation, *J. Nucl. Mater.* 367–370 (2007) 423–427.
- [18] W. Xu, L. Li, J.A. Valdez, et al., Effect of nano-oxide particle size on radiation resistance of iron-chromium alloys, *J. Nucl. Mater.* 469 (2016) 72–81.
- [19] P. Song, Z. Zhang, K. Yabuuchi, et al., Helium bubble formation behavior in ODS ferritic steels with and without simultaneous addition of Al and Zr, *Fusion Eng. Des.* 125 (2017) 396–401.
- [20] M.B. Toloczko, F.A. Garner, V.N. Voevodin, et al., Ion-induced swelling of ODS ferritic alloy MA957 tubing to 500 dpa, *J. Nucl. Mater.* 453 (2014) 323–333.
- [21] F.A. Garner, M.B. Toloczko, B.H. Sencer, Comparison of swelling and irradiation creep behavior of fcc-austenitic and bcc-ferritic/martensitic alloys at high neutron exposure, *J. Nucl. Mater.* 276 (2000) 123–142.
- [22] L. Fave, M.A. Pouchon, M. Döbeli, et al., Helium ion irradiation induced swelling and hardening in commercial and experimental ODS steels, *J. Nucl. Mater.* 445 (2014) 235–240.
- [23] A. Kimura, R. Kasada, R. Sugano, et al., Annealing behavior of irradiation hardening and microstructure in helium-implanted reduced activation martensitic steel, *J. Nucl. Mater.* 283–287 (2000) 827–831.
- [24] M. Roldán, P. Fernández, J. Rams, et al., Comparative study of helium effects on EU-ODS EUROFER and EUROFER97 by nanoindentation and TEM, *J. Nucl. Mater.* 460 (2015) 226–234.
- [25] H. Zhang, C. Zhang, Y. Yang, et al., Irradiation hardening of ODS ferritic steels under helium implantation and heavy-ion irradiation, *J. Nucl. Mater.* 455 (2014) 349–353.
- [26] C. Heintze, F. Bergner, M. Hernández-Mayoral, et al., Irradiation hardening of Fe-9Cr-based alloys and ODS Eurofer: Effect of helium implantation and iron-ion irradiation at 300 °C including sequence effects, *J. Nucl. Mater.* 470 (2016) 258–267.
- [27] H. Kishimoto, K. Yutani, R. Kasada, et al., Helium cavity formation research on oxide dispersed strengthening (ODS) ferritic steels utilizing dual-ion irradiation facility, *Fusion Eng. Des.* 81 (2006) 1045–1049.
- [28] R. Schaublin, Y.L. Chiu, Effect of helium on irradiation-induced hardening of iron: A simulation point of view, *J. Nucl. Mater.* 362 (2007) 152–160.
- [29] L. Peng, Y. Dai, Helium-induced hardening effect in ferritic/martensitic steels F82H and Optimax-A irradiated in a mixed spectrum of high energy protons and spallation neutrons, *J. Nucl. Mater.* 417 (2011) 996–1000.
- [30] R. Kasada, T. Morimura, A. Hasegawa, et al., Effect of helium implantation on mechanical properties and microstructure evolution of reduced-activation 9Cr-2W martensitic steel, *J. Nucl. Mater.* 299 (2001) 83–89.
- [31] S.J. Zinkle, N.M. Ghoniem, Operating temperature windows for fusion reactor structural materials, *Fusion Eng. Des.* 51–52 (2000) 55–71.
- [32] P. Dou, A. Kimura, T. Okuda, et al., Polymorphic and coherency transition of Y-Al complex oxide particles with extrusion temperature in an Al-alloyed high-Cr oxide dispersion strengthened ferritic steel, *Acta Mater.* 59 (2011) 992–1002.
- [33] P. Dou, A. Kimura, R. Kasada, et al., TEM and HRTEM study of oxide particles in an Al-alloyed high-Cr oxide dispersion strengthened steel with Zr addition, *J. Nucl. Mater.* 444 (2014) 441–453.
- [34] S. Ukai, T. Nishida, H. Okada, et al., Development of oxide dispersion strengthened ferritic steels for FBR core application, (I) Improvement of mechanical properties by recrystallization processing, *J. Nucl. Sci. Technol.* 34 (1997) 256–263.
- [35] A. Kohyama, Y. Katoh, M. Ando, et al., A new multiple beams-material interaction research facility for radiation damage studies in fusion materials, *Fusion Eng. Des.* 51–52 (2000) 789–795.
- [36] <http://www.srim.org>.
- [37] A. Xu, C. Beck, D.E.J. Armstrong, et al., Ion-irradiation-induced clustering in W-Re and W-Re-Os alloys: A comparative study using atom probe tomography and nanoindentation measurements, *Acta Mater.* 87 (2015) 121–127.
- [38] K. Morishita, R. Sugano, B.D. Wirth, et al., Thermal stability of helium-vacancy clusters in iron, *Nucl. Instrum. Methods Phys. Res., Sect. B* 202 (2003) 76–81.
- [39] H. Trinkaus, B.N. Singh, Helium accumulation in metals during irradiation – where do we stand? *J. Nucl. Mater.* 323 (2003) 229–242.
- [40] K. Yutani, R. Kasada, H. Kishimoto, et al., Irradiation hardening and microstructure evolution of ion-irradiated ODS ferritic steels, *J. ASTM Int. (JAI)* 4 (2007) 1–9.
- [41] I.-S. Kim, J.D. Hunn, N. Hashimoto, et al., Defect and void evolution in oxide dispersion strengthened ferritic steels under 3.2 MeV Fe^{+} ion irradiation with simultaneous helium injection, *J. Nucl. Mater.* 280 (2000) 264–274.
- [42] Z. Yao, M. Hernández-Mayoral, M.L. Jenkins, et al., Heavy-ion irradiations of Fe and Fe-Cr model alloys Part 1: Damage evolution in thin-foils at lower doses, *Philos. Mag.* 88 (2008) 2851–2880.
- [43] G.S. Was, *Fundamentals of Radiation Materials Science*, Springer, Berlin Heidelberg, New York, 2007.
- [44] C. Lu, Z. Lu, X. Wang, et al., Enhanced radiation-tolerant oxide dispersion strengthened steel and its microstructure evolution under helium-implantation and heavy-ion irradiation, *Sci. Rep.* 7 (2017) 40343.
- [45] L. Yang, Y. Yang, Y. Wu, et al., The ferrite/oxide interface and helium management in nanostructured ferritic alloys from the first principles, *Acta Mater.* 103 (2016) 474–482.
- [46] J. Ribis, Y. de Carlan, Interfacial strained structure and orientation relationships of the nanosized oxide particles deduced from elasticity-driven morphology in oxide dispersion strengthened materials, *Acta Mater.* 60 (2012) 238–252.
- [47] W.D. Nix, H. Gao, Indentation size effects in crystalline materials: A law for strain gradient plasticity, *J. Mech. Phys. Solids* 46 (1998) 411–425.
- [48] G.M. Pharr, E.G. Herbert, Y. Gao, The indentation size effect: A critical examination of experimental observations and mechanistic interpretations, *Annu. Rev. Mater. Res.* 40 (2010) 271–292.
- [49] D.G. Morris, M.A. Muñoz-Morris, Nanoprecipitation of oxide particles and related high strength in oxide-dispersion-strengthened iron-aluminum-chromium intermetallics, *Acta Mater.* 61 (2013) 4636–4647.
- [50] Y. Ha, A. Kimura, Effect of recrystallization on ion-irradiation hardening and microstructural changes in 15Cr-ODS steel, *Nucl. Instrum. Methods Phys. Res., Sect. B* 365 (2015) 313–318.
- [51] A. Kimura, T. Morimura, M. Narui, et al., Irradiation hardening of reduced activation martensitic steels, *J. Nucl. Mater.* 233–237 (1996) 319–325.
- [52] A. Kimura, R. Sugano, Y. Matsushita, et al., Thermal helium desorption behavior in advanced ferritic steels, *J. Phys. Chem. Solids* 66 (2005) 504–508.
- [53] J.T. Busby, M.C. Hash, G.S. Was, The relationship between hardness and yield stress in irradiated austenitic and ferritic steels, *J. Nucl. Mater.* 336 (2005) 267–278.
- [54] R. Nakai, K. Yabuuchi, S. Nogami, et al., The effect of voids on the hardening of body-centered cubic Fe, *J. Nucl. Mater.* 471 (2016) 233–238.
- [55] M. Cui, J. Wang, Z. Wang, et al., Helium irradiation induced hardening in MNHS steels, *Nucl. Instrum. Methods Phys. Res., Sect. B* 406 (2017) 611–617.
- [56] S.M. Hafez Haghighat, R. Schaublin, Molecular dynamics modeling of cavity strengthening in irradiated iron, *J. Comput. Aided Mater. Des.* 14 (2007) 191–201.
- [57] A. Kimura, R. Kasada, K. Morishita, et al., High resistance to helium embrittlement in reduced activation martensitic steels, *J. Nucl. Mater.* 307–311 (2002) 521–526.